

Chemical Science

Accepted Manuscript

This article can be cited before page numbers have been issued, to do this please use: Y. Jiang, R. Wang, P. Xiong, Y. Liu, H. Li, L. Zhang, Y. You and C. Zhang, *Chem. Sci.*, 2026, DOI: 10.1039/D5SC09186A.



This is an Accepted Manuscript, which has been through the Royal Society of Chemistry peer review process and has been accepted for publication.

Accepted Manuscripts are published online shortly after acceptance, before technical editing, formatting and proof reading. Using this free service, authors can make their results available to the community, in citable form, before we publish the edited article. We will replace this Accepted Manuscript with the edited and formatted Advance Article as soon as it is available.

You can find more information about Accepted Manuscripts in the [Information for Authors](#).

Please note that technical editing may introduce minor changes to the text and/or graphics, which may alter content. The journal's standard [Terms & Conditions](#) and the [Ethical guidelines](#) still apply. In no event shall the Royal Society of Chemistry be held responsible for any errors or omissions in this Accepted Manuscript or any consequences arising from the use of any information it contains.

Solid Dual-Salt Plastic Crystal Electrolyte Enabling Rapid Ion Transfer and Stable Interphases for High-Performance Solid-State Sodium Ion Batteries

Yang Jiang,^a Rui Wang,^a Peng Xiong,^a Yangyang Liu,^a Hongbao Li,^a Longhai Zhang,^{*a}

Ya You,^b and Chaofeng Zhang^{*a}

^a Institutes of Physical Science and Information Technology, Leibniz International Joint Research Center of Materials Sciences of Anhui Province, Anhui University, Hefei 230601, China.

E-mail: cfz@ahu.edu.cn, zlhedu@ahu.edu.cn

^b State Key Laboratory of Advanced Technology for Materials Synthesis and Processing, Wuhan University of Technology, Wuhan 430070, China.



Abstract: As promising next-generation energy storage systems, solid-state sodium ion batteries (SIBs) are hindered by the low ionic conductivity of their solid electrolytes and poor interfacial compatibility. Here, we developed a solid dual-salt plastic crystal electrolyte (PCE) composed of succinonitrile (SN), fluoroethylene carbonate (FEC), and dual salts (NaClO_4 and NaBF_4). The synergistic redox reactions of FEC and BF_4^- form a robust, F- and B-rich interphase at electrode/electrolyte interfaces, which significantly enhances interfacial stability and minimizes side reactions that cause cell degradation. Meanwhile, the derived interphase combined with SN's intrinsic oxidation stability, endows the PCE with high-voltage tolerance (≥ 4.75 V), enabling stable operation with high-voltage cathodes. Furthermore, SN's high polarity and plastic character facilitate Na-salt dissociation and optimize interfacial contact, while the competitive coordination of BF_4^- with Na^+ over ClO_4^- increases the free Na^+ , synergistically enhancing ionic conductivity to 3.79 mS cm^{-1} . Consequently, the dual-salt PCE enables high-performance SIBs when paired with multiple electrode materials such as $\text{Na}_3\text{V}_4(\text{PO}_4)_3$, Prussian white, $\text{Na}_3\text{V}_2(\text{PO}_4)_2\text{F}_3$ cathodes, and hard carbon anode. They deliver exceptional cycling stability (over 2500 cycles), rate performance (up to 60 C), specific capacity (163.9 mAh g^{-1}), and operating voltage (≥ 4.0 V). Moreover, the hard carbon|| $\text{Na}_3\text{V}_4(\text{PO}_4)_3$ full cell maintains stable cycling at 10 C over 100 cycles, highlighting its promise for practical applications.

Keywords

solid-state sodium ion batteries, dual-salt plastic crystal electrolyte, F- and B-rich interphase, high-voltage tolerance



1. Introduction

As a promising alternative of lithium-ion batteries (LIBs), sodium-ion batteries (SIBs) are highly competitive due to the high natural abundance and low cost of sodium.¹⁻⁴ However, the traditional liquid electrolytes (e.g. carbonate- and ether-based) commonly used in SIBs always suffer inherent drawbacks including leakage, volatility, and flammability, which raise serious safety risks.⁵⁻⁸ Solid-state electrolytes (SSEs) offer a promising solution with their inherent safety features and potential for higher energy density. Nevertheless, the practical applications of SSEs are still challenged by their low ionic conductivity, high interfacial resistance, and undesirable interfacial side reactions, which result in unsatisfactory battery performance.^{9, 10} Therefore, the development of advanced SSEs that enable efficient and stable operation in SIBs remains a significant challenge.^{11, 12}

The plastic crystal electrolyte (PCE) is a novel solid-state electrolyte composed of a metal salt and a plastic crystal. These systems are known for their strong solvation capability and fast ionic transport behaviors. Among various plastic crystals, succinonitrile (SN, NC-CH₂-CH₂-CN) stands out as a highly polar non-ionic plastic crystal molecule. It maintains a plastic crystalline phase between -40 and 60 °C, which allows it to remain a solid state and exhibit high safety at room temperature.¹³⁻¹⁵ Furthermore, its high polarity and high dielectric constant ($\epsilon \approx 55$) promote salts dissociation and support a high concentration of charge carriers. These enable SN-based PCE to achieve high ionic conductivities of $\approx 10^{-3} \text{ S cm}^{-1}$ even at room temperature, making them highly attractive for solid-state battery applications. Additionally, SN



possesses remarkable oxidation resistance, which makes it suitable for high-voltage battery systems.¹⁶⁻¹⁹

However, SN molecule suffers from poor reduction stability. In contact with Na metal, the cyano group ($-C\equiv N$) inside could catalyze spontaneous polymerization, forming detrimental by-products. This reaction degrades the electrolyte/electrode interface and leads to irreversible interfacial corrosion, severely compromising the cycling lifespan.²⁰⁻²³ Furthermore, SN typically exhibits insufficient mechanical strength which would further exacerbate by the plasticizing effect of high-concentration sodium salts. Although PCE have been utilized as electrode/electrolyte interphase layers or electrolyte additives in SIBs, their widespread practical application in rechargeable sodium-metal systems remains limited. Therefore, to enable practical deployment, PCE must therefore address three critical challenges including low mechanical strength, poor reduction stability, and side reactions with Na metal.^{24, 25}

To overcome the poor reduction stability and mechanical strength of SN-based PCE, this work develops a solid dual-salt PCE film incorporating SN, fluoroethylene carbonate (FEC), dual-salt system ($NaClO_4$ and $NaBF_4$), and glass fiber matrix. The synergistic redox reactions of FEC and BF_4^- lead to a robust, borate- and fluoride-rich interphase on both electrode/electrolyte interfaces, which significantly enhances the interface stability and minimizes side reactions that cause cell degradation. The derived robust interphase combined with intrinsic oxidation stability of SN further endows the electrolyte with high-voltage tolerance up to 4.75 V, enabling stable operation with high-voltage cathodes. SN's high polarity and plastic character can facilitate Na-salt



dissociation and enhance interfacial compatibility, while the competitive coordination of BF_4^- with Na^+ over ClO_4^- increases the free Na^+ , synergistic enhancing the ionic conductivity to 3.79 mS cm^{-1} . The glass fiber matrix as the substrate provides critical mechanical reinforcement. As a result, the $\text{Na}||\text{Na}_3\text{V}_4(\text{PO}_4)_3$ cell with dual-salt PCE exhibits stable cycling over 2500 cycles and superior rate performance (up to 60 C). When paired with a hard carbon anode, the hard carbon $||\text{Na}_3\text{V}_4(\text{PO}_4)_3$ full cell also maintains exceptional cycling stability over 100 cycles at 10 C. Moreover, the dual-salt PCE demonstrates good compatibility with Prussian white and $\text{Na}_3\text{V}_2(\text{PO}_4)_2\text{F}_3$ cathodes, delivering a high capacity of 163.9 mAh g^{-1} and an operating voltage over 4.0 V, respectively. This work presents a novel design of PCE with high interface stability and compatibility for high-performance solid-state SIBs.

2. Experimental section

Preparation of solid dual-salt PCE

A liquid PCE was first obtained by mixing the SN (3.6 g, Aladdin), NaClO_4 (0.9 g, Aladdin), NaBF_4 (0.05 g, Aladdin), and FEC (80 μL , Aladdin) at 65°C . The resulting liquid PCE was then cast onto a glass fiber (Whatman) reinforcement, and stand for 12 h to complete the solidification process, forming the solid dual-salt PCE. For comparison, the solid NaClO_4 -PCE and NaBF_4 -PCE with individual Na salt (NaClO_4 or NaBF_4) were prepared using the same procedure. All processes of solid PCE preparation were conducted in an Ar-filled glove box (Mikrouna, $[\text{O}_2] < 0.01 \text{ ppm}$, $[\text{H}_2\text{O}] < 0.01 \text{ ppm}$).

Preparation of electrode



In this study, four electrode materials including $\text{Na}_3\text{V}_4(\text{PO}_4)_3$, Prussian white, $\text{Na}_3\text{V}_2(\text{PO}_4)_2\text{F}_3$ cathodes, and hard carbon anode were used to investigate the PCE's compatibility. Among them, $\text{Na}_3\text{V}_4(\text{PO}_4)_3$, $\text{Na}_3\text{V}_2(\text{PO}_4)_2\text{F}_3$, and hard carbon were purchased from Guangdong Canrd New Energy Technology Co., Ltd. Prussian white was prepared according to the previously reported method²⁶. Afterward, these electrodes were fabricated by grinding and mixing 65 wt% active material, 5 wt% conductive carbon black, 5 wt% polyvinylidene fluoride (PVDF) binder, and 25 wt% dual-salt plastic crystal in an N-methyl-2-pyrrolidone (NMP) solvent to form a homogeneous slurry. This slurry was then cast onto carbon-coated aluminum foil (Al@C) and finally dried at 50 °C for over 24 h. NVP active material loading in the range of 1.2-1.5 mg cm⁻², PW active material loading in the range of 1-1.2 mg cm⁻². NVPF active material loading in the range of 1.2-1.4 mg cm⁻². HC active material loading in the range of 1.1-1.3 mg cm⁻².

Material characterization

PCEs were observed by optical microscope (YM710TR, Yuescope) and cryogenic scanning electron microscope (Cryo-SEM, HITACHI Regulus8100). The Fourier transform infrared (FTIR, Thermo Fisher Nicolet is5) spectra was performed at ambient temperature. Raman spectra were observed by using a Renishaw inVia-Reflex instrument. Deep etching X-ray photoelectron spectroscopy (XPS, ESCALAB 250Xi) analysis was conducted using an instrument on the surface of cycled $\text{Na}_3\text{V}_4(\text{PO}_4)_3$ cathode and sodium metal anode.

Electrochemical measurements



All CR-2032 type coin cells were assembled in a glove box (Mikrouna), and then tested using PARSTATMC electrochemical workstation (PMC1000) and NEWARE tester (5 V/10 mA, Shenzhen, China). Among them, the linear sweep voltammetry (LSV) of PCE was measured using stainless steel||Na cell at 0.1 mV s⁻¹. The corresponding ionic conductivity (σ) and Arrhenius activation energy (E_a) were conducted at different temperatures through electrochemical impedance spectroscopy (EIS) and calculated by the following equation:

$$\sigma = L/RS$$

where L represents the separator thickness, R and S are the bulk resistance and electrode area, respectively.

$$R_{ct}^{-1} = Ae^{-E_a/RT}$$

where R_{ct} stands for the interface resistance, A, R, and T denote the frequency factor, gas constant, and absolute temperature, respectively. The frequency range of the EIS test is from 10 to 10⁵.

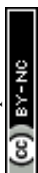
The Na⁺ transference number (t_{Na^+}) of PCE was tested according to the chronoamperometry measurement and calculated by the formula:

$$t_{Na^+} = I_S(\Delta V - I_0 R_0) / I_0(\Delta V - I_S R_S)$$

where I_0 , I_S , R_0 , and R_S stand for the current and resistance before and after polarization. ΔV corresponds to the applied polarization voltage (10 mV).

Galvanostatic charge/discharge profiles, cycling performance, and rate capability of the assembled cells was conducted on a NEWARE tester.

In addition, the assembly of Pouch cells: The NVP cathode (5×5 cm) , glass fiber



(Whatman, GF/A), and dual-salt PCE were used as the working electrode, separator, and electrolyte, respectively. Subsequently, the hard carbon (HC) is used as the anode (5×5 cm) for HC//NVP pouch cells.

Theoretical calculations

The Gaussian 16 program was employed to calculate the highest occupied molecular orbitals (HOMO), lowest unoccupied molecular orbitals (LUMO), electrostatic potential (ESP), and binding energy for the various molecular models based on the B3LYP functional method and 6-311+G(b,p) basis set.

3. Results and discussion

We selected SN and NaClO₄ as the basic solid-state PCE due to their high ionic conductivity and superior interfacial compatibility. Meanwhile, FEC and NaBF₄ were introduced as interfacial film-forming additives to minimize the reactivity of SN toward Na metal and reinforce the PCE's oxidation stability, contributing to stable cycling and higher voltage operation in SIBs. Therefore, a solid dual-salt PCE composed of SN, FEC, NaClO₄, and NaBF₄ was developed, as shown in **Fig. 1a and b**. For comparison, the solid-state PCE with individual Na salt (NaClO₄ or NaBF₄) were prepared to highlight the advantages of the dual-salt system. It should be noted that the poor mechanical strength of solid-state dual-salt PCE limits its processability and practical application. To address this, a glass fiber separator (GFs) was employed as the mechanical reinforcing framework, and the melted dual-salt PCE was poured and re-solidified inside, resulting in a GFs supported solid dual-salt PCE film. The optical photographs confirm the successful solidification and uniform filler distribution (**Fig. 1c and d**). The cross-section cryogenic scanning electron microscope (Cryo-SEM)

View Article Online
DOI: 10.1039/D5SC09186A



further verified the filled microstructure and the film thickness of ≈ 0.5 mm (**Fig. 1e and f**). Afterward, the energy-dispersive X-ray spectroscopy (EDS) mapping revealed a homogeneous distribution of the key elements (Na, C, O, N, F, Cl, and B) throughout the film (**Fig. 1g**), indicating the uniform integration of SN, FEC, NaClO_4 , and NaBF_4 . Fourier transform infrared spectrometer (FT-IR) and Raman spectra further validated this, just as shown in **Fig. 1h and i**. The distinct peaks of $\text{C}\equiv\text{N}$ (2253 cm^{-1}), $\text{C}=\text{O}$ (1830 cm^{-1}), $\text{C}-\text{F}$ (1002 cm^{-1}), ClO_4^- (1084 cm^{-1}), and $\text{B}-\text{F}$ (763 cm^{-1}) were observed, which originate from SN, FEC, NaClO_4 , and NaBF_4 .²⁷ Meanwhile, the Raman spectra exhibited the characteristic peaks of $\text{C}\equiv\text{N}$, ClO_4^- , and BF_4^- as well.²⁸

Afterward, the highest occupied molecular orbital (HOMO) and lowest unoccupied molecular orbital (LUMO) energy levels of SN, FEC, NaClO_4 , and NaBF_4 were calculated to compare their oxidation and reduction potential (**Fig. 1j**). As for the HOMO levels, SN and NaBF_4 manifest the energy levels of -8.372 and -8.111 eV, respectively, which are lower than those of FEC (-7.479 eV) and NaClO_4 (-6.355 eV), indicating their higher anti-oxidation potential. Additionally, dual-salt system (NaClO_4 and NaBF_4) exhibited lower LUMO energy levels (-2.185 and -1.997 eV, respectively) than SN (-1.256 eV) and FEC (-0.915 eV), indicating higher reactivity toward reduction at Na anode. Therefore, the preferential reduction of dual-salt system (NaClO_4 and NaBF_4) forms a protective inorganic-rich solid-electrolyte interphase (SEI) layer, which could shield SN from the Na metal, effectively enhancing SN's reduction stability and mitigating undesirable side reactions.

According to the electrochemical impedance spectroscopy (EIS) of PCE with



different Na salt systems (dual salts, NaClO₄, or NaBF₄) at room temperature (**Fig. 2a**), the dual-salt PCE exhibits the highest ionic conductivity of $3.79 \times 10^{-3} \text{ S cm}^{-1}$, significantly surpassing those of NaClO₄-PCE ($1.38 \times 10^{-3} \text{ S cm}^{-1}$) and NaBF₄-PCE ($0.023 \times 10^{-3} \text{ S cm}^{-1}$). This enhancement could be attributed to the increased number of free Na⁺ in the dual-salt PCE, where BF₄[−] competes with ClO₄[−] for Na⁺ coordination (**Fig. S1**), effectively disrupting the stable ion-pair structure in the single-salt system and increasing the free Na⁺ concentration. Subsequently, further Arrhenius plots show the dual-salt PCE with a lower activation energy (E_a , 0.175 eV) than that of NaClO₄-PCE (0.393 eV), indicating its lower energy barrier for Na⁺ transport inside (**Fig. 2b and Fig. S2**). Moreover, the dual-salt PCE demonstrates an elevated Na⁺ transport number of 0.68 (**Fig. 2c**), exceeding the NaClO₄-PCE (0.54, **Fig. 2d**). Furthermore, the electrochemical stability window of dual-salt PCE, NaClO₄-PCE, and NaBF₄-PCE was analyzed by linear sweep voltammetry (LSV) and electrochemical floating analysis (EFA). As shown in **Fig. 2e**, dual-salt PCE and NaBF₄-PCE exhibit high oxidation potential exceeding 4.75 and 5.0 V vs. Na⁺/Na, respectively. In contrast, the NaClO₄-PCE without NaBF₄ exhibits an oxidation potential starting around 4.6 V vs. Na⁺/Na. Therefore, the enhanced anti-oxidation potential could be attributed to the NaBF₄. High oxidative stability is crucial for stable operation of high-voltage cathodes like Na₃V₂(PO₄)₂F₃. To verify this, the Na||Na₃V₂(PO₄)₂F₃ battery was charged to 4.8 V, just as shown in **Fig. 2f**. The leakage current at 4.7 V still remains below 20 μA, which is well consistent with the LSV result, further demonstrating dual-salt PCE's outstanding oxidation stability and high-voltage compatibility.



Apart from the oxidation stability and high-voltage compatibility for cathode, the impact of dual-salt PCE on the stability of Na metal anode was further investigated. Na symmetrical cells with solid-state PCE film were assembled to evaluate the interfacial behavior between PCE and Na metal. As displayed in **Fig. 3a and b**, Na symmetrical cell can stably cycle over 500 h at $0.25 \text{ mA cm}^{-2}/0.125 \text{ mAh cm}^{-2}$ with a small polarization voltage (**Fig. S3**), indicating the high compatibility of dual-salt PCE toward Na metal and a stable Na plating/stripping behavior. In contrast, the cell with NaClO_4 -PCE fails after only 100 h, accompanied by a continues increase in polarization. The NaBF_4 -PCE exhibited a higher overpotential throughout its operation and failed after 200 h. Even at a higher current density of 1 mA cm^{-2} and 0.5 mAh cm^{-2} , the dual-salt PCE still stably cycle approximately 200 h and exhibits an even and dense surface (**Fig. S4**).

To investigate the interfacial stability between dual-salt PCE and Na metal anode, the SEI layer on the cycled Na metal anode was analyzed using deep etching X-ray photoelectron spectroscopy (XPS). As shown in **Fig. 3c**, the F1s spectrum exhibits a characteristic peak for inorganic NaF at 683.8 eV, which could originate from the decomposition of FEC and BF_4^- anions.²⁹⁻³¹ Owing to its low adsorption energy with SN, NaF serves as a crucial component in SEI to inhibit side reactions between SN and Na. In addition, the B1s peak was detected and deconvoluted into three peaks corresponding to B-F (193.6 eV), NaB_xO_y (192.2 eV), and B-O (190.7 eV) species (**Fig. 3d**), confirming the incorporation of both fluorine and boron inside.³²⁻³⁴ Note that the intensities of the NaF and NaB_xO_y signals both increased and became dominant after



sputtering (**Fig. 3c and d**), while other component signals decreased in the F1s spectrum (**Fig. 3c**), indicating the formation of an inorganic-rich, F/B-containing SEI layer. Such mechanically robust, F/B-rich SEI layer significantly improves the interfacial stability between the dual-salt PCE and Na metal anode. Afterward, the LUMO energy levels of $\text{Na}^+\text{-SN}$, $\text{Na}^+\text{-FEC}$, and $\text{Na}^+\text{-BF}_4^-$ were computed to understand the formation of the F/B-containing SEI, just as shown in **Fig. 3e**. The $\text{Na}^+\text{-FEC}$ and $\text{Na}^+\text{-BF}_4^-$ both exhibit lower LUMO energies (-2.43 and -1.99 eV, respectively) than that of $\text{Na}^+\text{-SN}$ (-1.95 eV), indicating that FEC and BF_4^- anions are more easily reduced on Na metal to generate NaF- and NaB_xO_y -rich layer, well consistent with the XPS results.

Benefiting from the high ionic conductivity, anti-oxidation/reduction stability, and comparability of solid-state dual-salt PCE film, corresponding Na||dual-salt PCE||NVP batteries were highly expected to exhibit superior performance. As displayed in **Fig. 4a and b** the Na||dual-salt PCE||NVP cell shows attractive rate capability within the rate range from 1 to 60 C. It delivers large discharge capacities of 114.7, 108.5, 104.6, 99.1, 93.1, and 76.6 mAh g⁻¹, respectively. Notably, when the rate returns to 1 C, a capacity of 112.9 mAh g⁻¹ can be achieved, highlighting its great reversibility. In contrast, Na||NVP with liquid electrolyte (LE, 1M NaClO₄ in EC:PC=1:1 Vol% with 5%FEC) and NaClO₄-PCE exhibits poor rate performance especially at a higher rate of 60 C, only 33.1 and 50.7 mAh g⁻¹ were retained, respectively. Subsequently, the cycling stability of Na||dual-salt PCE||NVP cell was evaluated at 2 C. Encouragingly, it remains



a capacity as high as 104.7 with 95.1% capacity retention after 100 cycles (**Fig. 4c and d**). The corresponding charge/discharge profiles further confirm its stability and well-defined plateaus. Importantly, even at 20 C and over 2500 cycles, this battery maintains a capacity of 75.6 mAh g⁻¹ (**Fig. 4e**). In contrast, Na||NVP cells with LE and NaClO₄-PCE fails after 1700 and 20 cycles, respectively. Furthermore, at a rate of 60 C, the cell with dual-salt PCE still cycle stably over 700 cycles (**Fig. S5 and S6**). To understand the superior stability, we focus on the cathode/electrolyte interface (CEI). Then the CEI formed on the surface of cycled NVP cathode was analyzed by deep etching XPS. As shown in **Fig. 4f and g**, the signals for inorganic NaF and NaB_xO_y were detected at 684.1 and 192.2 eV before and after sputtering, which are derived from the decomposition of FEC and BF₄⁻ anions. In addition to NaF and NaB_xO_y, trace amounts of Na₃N (398.9 eV) as a known Na⁺ conductor were observed on the cathode surface as well (**Fig. 4f**).³⁵ This inorganic-rich CEI composed of highly stable NaF/NaB_xO_y and conductive Na₃N can be effective barrier for stable cathode/electrolyte interface (**Fig. 4g**).

To evaluate the compatibility and applicability of the solid-state dual-salt PCE, several representative electrodes including Prussian white (PW), Na₃V₂(PO₄)₂F₃ (NVPF), hard carbon (HC) were investigated. As shown in **Fig. 5a**, the Na||PW cell with solid-state dual-salt PCE delivers a high discharge capacity of 163.9 mAh g⁻¹ at 0.1 C, accompanied by the typical charge/discharge behaviors of PW cathode. Notably, even at higher rates of 0.5 C and 1 C, the cell can stably cycle over 100 cycles and



maintain exceptionally high capacities of 142.9 and 126.6 mAh g⁻¹, respectively (**Fig. 5b**). Additionally, rate capability was further measured at rates from 0.5 to 5 C, with capacities of 142.3, 126.6, 109.1, 100.5, and 86.1 mAh g⁻¹, respectively (**Fig. 5c and Fig. S7**). When the rate is returned to 0.5 C, the capacity recovers to 142 mAh g⁻¹, highlighting remarkable reversibility. Even paired with high-voltage NVPF cathode, as displayed in **Fig. 5d**, the Na||NVPF cell offer a discharge capacity of 127.5 mAh g⁻¹ with an operating voltage over 4.0 V. Meanwhile, the cell presents superior cyclability (89.7 mAh g⁻¹ after 100 cycles at 1 C) and rate capability (**Fig. 5e and f and Fig. S8**). Beyond cathodes, hard carbon anode, as a critical component for full cells, was also investigated (**Fig. 5g**). The Na||HC cell delivers a discharge capacity of 320.4 mAh g⁻¹ at 0.1 C along with typical charge/discharge behaviors for hard carbon. Additionally, the cells exhibit a stable cycling over 300 cycles at 1 C and 2 C, maintaining capacities of 146.5 and 124.6 mAh g⁻¹, respectively (**Fig. 5h**). Afterward, to access practical applications of solid-state dual-salt PCE, a HC||Na₃V₂(PO₄)₃ full cell was assembled. The full cell exhibits exceptional cycling stability at 10 C with minimal capacity decay over 100 cycles (**Fig. 5i and Fig. S9**). Additionally, the pouch cell effectively powers a LED lamp even after repeated flattening and folding (**Fig. S10**).

4. Conclusion

In summary, this work develops a solid dual-salt PCE film incorporating SN, FEC, dual-salt system (NaClO₄ and NaBF₄), and glass fiber matrix. The synergistic redox reactions of FEC and BF₄⁻ lead to a robust, borate- and fluoride-rich interphase on both electrode/electrolyte interfaces, which significantly enhances the interface stability and



minimizes side reactions that cause cell degradation. The derived robust interphase combined with intrinsic oxidation stability of SN further endows the electrolyte with high-voltage tolerance up to 4.75 V, enabling stable operation with high-voltage cathodes. SN's high polarity and plastic character can facilitate Na-salt dissociation and enhance interfacial compatibility, while the competitive coordination of BF_4^- with Na^+ over ClO_4^- increases the free Na^+ , synergistically enhancing the ionic conductivity to 3.79 mS cm^{-1} . The glass fiber matrix as the substrate provides critical mechanical reinforcement. Consequently, the $\text{Na}||\text{Na}_3\text{V}_4(\text{PO}_4)_3$ cell with solid dual-salt PCE exhibits stable cycling over 2500 cycles and superior rate performance (60 C). When coupled with a hard carbon (HC) anode, the $\text{HC}||\text{Na}_3\text{V}_4(\text{PO}_4)_3$ full cell also delivers stable cycling over 100 cycles at 10 C. Moreover, the solid dual-salt PCE demonstrates good compatibility with Prussian white and $\text{Na}_3\text{V}_2(\text{PO}_4)_2\text{F}_3$ cathodes, both enabling high-performance solid-state SIBs. This work presents a novel design of PCE with high interface stability and compatibility for high-performance solid-state SIBs.

Author contributions

Y. J., L. H. Z., and C. F. Z. designed this work. Y. J., Y. Y. L., and R. W. carried out the synthesis and characterization of the materials. P. X., H. B. L., and Y. Y. performed the data analysis and DFT calculations. Y. Y., L. H. Z., and C. F. Z. co-wrote and supervised the manuscript.

Conflicts of interest

The authors declare no conflict of interest.

Data Availability Statement



The data that support the findings of this study are available from the corresponding author upon reasonable request.

Acknowledgements

The authors thank the financial support from the National Key Research and Development Program of China (2023YFB2406100), the National Natural Science Foundation of China (52172173, 52302205), Excellent Research and Innovation Team Project of Anhui Province (2022AH010001). Numerical computations were performed on Hefei advanced computing center.

Notes and references

1. C. Matei Ghimbeu, A. Beda, B. Réty, H. El Marouazi, A. Vizintin, B. Tratnik, L. Simonin, J. Michel, J. Abou-Rjeily and R. Dominko, *Adv. Energy Mater.*, 2024, **14**, 2303833.
2. J. Wang, Y.-F. Zhu, Y. Su, J.-X. Guo, S. Chen, H.-K. Liu, S.-X. Dou, S.-L. Chou and Y. Xiao, *Chem. Soc. Rev.*, 2024, **53**, 4230-4301.
3. Y. Wu, W. Shuang, Y. Wang, F. Chen, S. Tang, X.-L. Wu, Z. Bai, L. Yang and J. Zhang, *Electrochem. Energy Rev*, 2024, **7**, 17.
4. J. Li, H. Hu, J. Wang and Y. Xiao, *Carbon Neutralization*, 2022, **1**, 96-116.
5. J. Xu, J. Zhang, T. P. Pollard, Q. Li, S. Tan, S. Hou, H. Wan, F. Chen, H. He, E. Hu, K. Xu, X.-Q. Yang, O. Borodin and C. Wang, *Nature*, 2023, **614**, 694-700.
6. Z. Zhang, Y. Li, R. Xu, W. Zhou, Y. Li, S. T. Oyakhire, Y. Wu, J. Xu, H. Wang, Z. Yu, D. T. Boyle, W. Huang, Y. Ye, H. Chen, J. Wan, Z. Bao, W. Chiu and Y. Cui, *Science*, 2022, **375**, 66-70.
7. S. Wan, K. Song, J. Chen, S. Zhao, W. Ma, W. Chen and S. Chen, *J. Am. Chem. Soc.*, 2023, **145**, 21661-21671.
8. Z. Yang, X.-Z. Zhou, Z.-Q. Hao, J. Chen, L. Li, Q. Zhao, W.-H. Lai and S.-L. Chou, *Angew. Chem. Int. Ed.*, 2024, **63**, e202313142.



9. H. Xu, D. Zhang, W. Wang, G. Yu, M. Zhu and Y. Liu, *Carbon Neutralization*, 2025, **4**, e70031.
10. J. Ren, H. Zhu, Y. Fang, W. Li, S. Lan, S. Wei, Z. Yin, Y. Tang, Y. Ren and Q. Liu, *Carbon Neutralization*, 2023, **2**, 339-377.
11. Z. Hu, L. Liu, X. Wang, Q. Zheng, C. Han and W. Li, *Adv. Funct. Mater.*, 2024, **34**, 2313823.
12. J. Wang, D. Yu, X. Sun, H. Wang and J. Li, *eScience*, 2024, **4**, 100252.
13. J.-Y. Hwang, S.-T. Myung and Y.-K. Sun, *Chem. Soc. Rev.*, 2017, **46**, 3529-3614.
14. Z. Lu, H. Yang, Y. Guo, P. He, S. Wu, Q.-H. Yang and H. Zhou, *Angew. Chem. Int. Ed.*, 2022, **61**, e202206340.
15. J. Chen, Z. Yang, X. Xu, Y. Qiao, Z. Zhou, Z. Hao, X. Chen, Y. Liu, X. Wu, X. Zhou, L. Li and S.-L. Chou, *Adv. Mater.*, 2024, **36**, 2400169.
16. S. Zhang, S. Li and Y. Lu, *eScience*, 2021, **1**, 163-177.
17. D. A. Rakov, F. Chen, S. A. Ferdousi, H. Li, T. Pathirana, A. N. Simonov, P. C. Howlett, R. Atkin and M. Forsyth, *Nat. Mater.*, 2020, **19**, 1096-1101.
18. Y. Yan, Z. Liu, T. Wan, W. Li, Z. Qiu, C. Chi, C. Huangfu, G. Wang, B. Qi, Y. Yan, T. Wei and Z. Fan, *Nat. Commun.*, 2023, **14**, 3066.
19. J. Huang, K. Wu, G. Xu, M. Wu, S. Dou and C. Wu, *Chem. Soc. Rev.*, 2023, **52**, 4933-4995.
20. W. Bao, Y. Zhang, L. Cao, Y. Jiang, H. Zhang, N. Zhang, Y. Liu, P. Yan, X. Wang, Y. Liu, H. Li, Y. Zhao and J. Xie, *Adv. Mater.*, 2023, **35**, 2304712.
21. Q. Wang, X. Xu, B. Hong, M. Bai, J. Li, Z. Zhang and Y. Lai, *Chem. Eng. J.*, 2022, **428**, 131331.
22. V. van Laack, F. Langer, A. Hartwig and K. Koschek, *ACS Omega*, 2023, **8**, 9058-9066.
23. J. Ma, M. Yu, M. Huang, Y. Wu, C. Fu, L. Dong, Z. Zhu, L. Zhang, Z. Zhang, X. Feng and H. Xiang, *Small*, 2024, **20**, 2305649.
24. Y. Liu, Y. Zhao, W. Lu, L. Sun, L. Lin, M. Zheng, X. Sun and H. Xie, *Nano Energy*, 2021, **88**, 106205.



25. J. Yu, Y. Zhang, T. Gao, X. Zhang, Y. Lv, Y. Zhang, C. Zhang and W. Liu, *Chem. Eng. J.*, 2024, **487**, 150646.
26. R. Sun and Y. You, *ACS Appl. Mater. Interfaces*, 2023, **15**, 44599-44606.
27. Y. Lu, Y. Cai, Q. Zhang, L. Liu, Z. Niu and J. Chen, *Chem. Sci.*, 2019, **10**, 4306-4312.
28. D. Reber, O. Borodin, M. Becker, D. Rentsch, J. H. Thienenkamp, R. Grissa, W. Zhao, A. Aribia, G. Brunklaus, C. Battaglia and R.-S. Kühnel, *Adv. Funct. Mater.*, 2022, **32**, 2112138.
29. P. Zou, C. Wang, Y. He and H. L. Xin, *Angew. Chem. Int. Ed.*, 2024, **63**, e202319427.
30. F. Feng, Z. Liu, Y. Yan, M. Gong, G. Wang, C. Chi, B. Qi, C. Huangfu, X. Yang, K. Cao, F. Meng, T. Wei and Z. Fan, *Small*, 2024, **20**, 2403275.
31. S. Weng, Y. Liu, S. Lu, J. Xu, J. Xue, H. Tu, Z. Wang, L. Liu, Y. Gao, G. Sun, H. Li and X. Wu, *Angew. Chem. Int. Ed.*, 2025, **64**, e202421602.
32. Z. Yang, J. Pan, H. Wu, K. Shi, Z. Chen, J. Li, W. Huang, T. Yang, Y. Hong, R. Zhang, Z. Lu, J. Li and Q. Liu, *Nano Energy*, 2025, **141**, 111083.
33. L. Gao, J. Chen, Q. Chen and X. Kong, *Sci. Adv.*, 2022, **8**, eabm4606.
34. X. Liu, J. Zhao, H. Dong, L. Zhang, H. Zhang, Y. Gao, X. Zhou, L. Zhang, L. Li, Y. Liu, S. Chou, W. Lai, C. Zhang and S. Chou, *Adv. Funct. Mater.*, 2024, **34**, 2402310.
35. A. Xu, L. Zhao, J. Yu, W. Deng, J. Li, H. Zhang, H. Xu and L. Xu, *Angew. Chem. Int. Ed.*, 2025, **64**, e202506058.



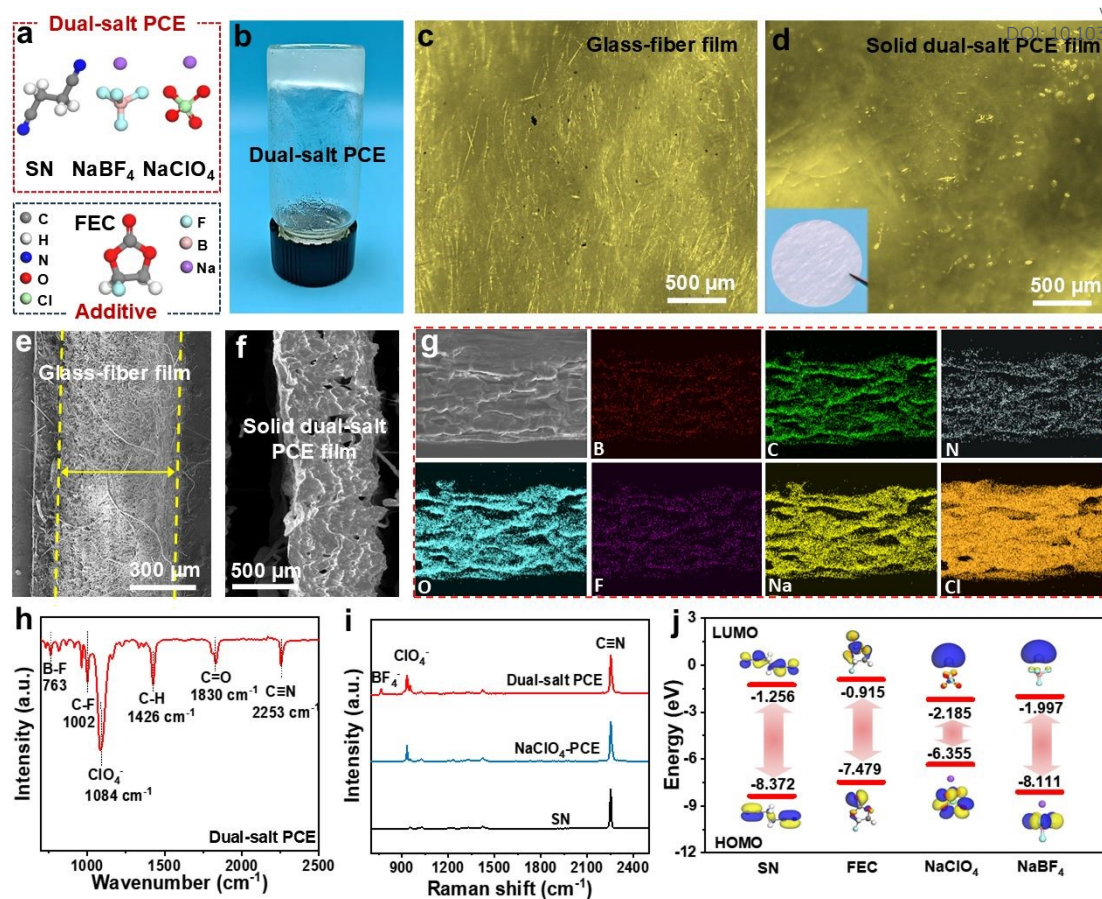


Fig. 1 (a) Schematic illustration of the dual-salt PCE design. (b) The optical photograph of the solid dual-salt PCE. (c and d) The optical photograph of GFs and GFs supported solid dual-salt PCE film. (e and f) Cryo-SEM images of GFs and GFs supported solid dual-salt PCE film. (g) Elemental mapping of the solid dual-salt PCE film. (h) FTIR of the dual-salt PCE. (i) Raman spectra of the dual-salt PCE, NaClO₄-PCE, and SN. (j) LUMO and HOMO values of SN, FEC, NaClO₄, and NaBF₄.



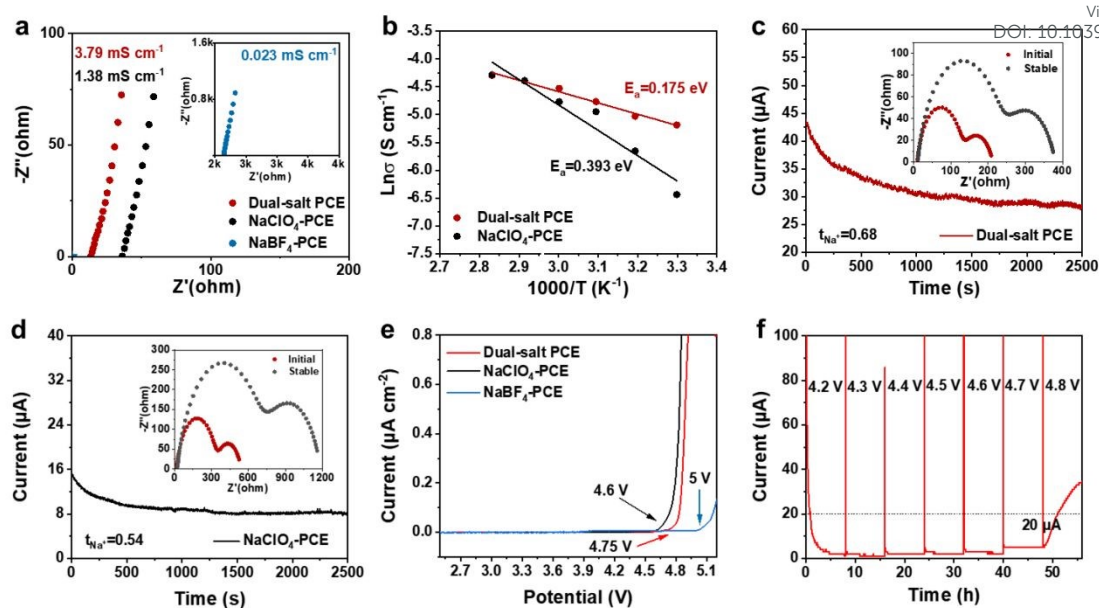


Fig. 2 (a) Ionic conductivity of the dual-salt PCE, NaClO_4 -PCE, and NaBF_4 -PCE. (b) Arrhenius plots of the dual-salt PCE and NaClO_4 -PCE. (c and d) The polarization profiles of the dual-salt PCE and NaClO_4 -PCE (Inset show the EIS plots before and after polarization). (e) LSV curves of the dual-salt PCE, NaClO_4 -PCE, and NaBF_4 -PCE. (f) Electrochemical floating analysis of the dual-salt PCE.



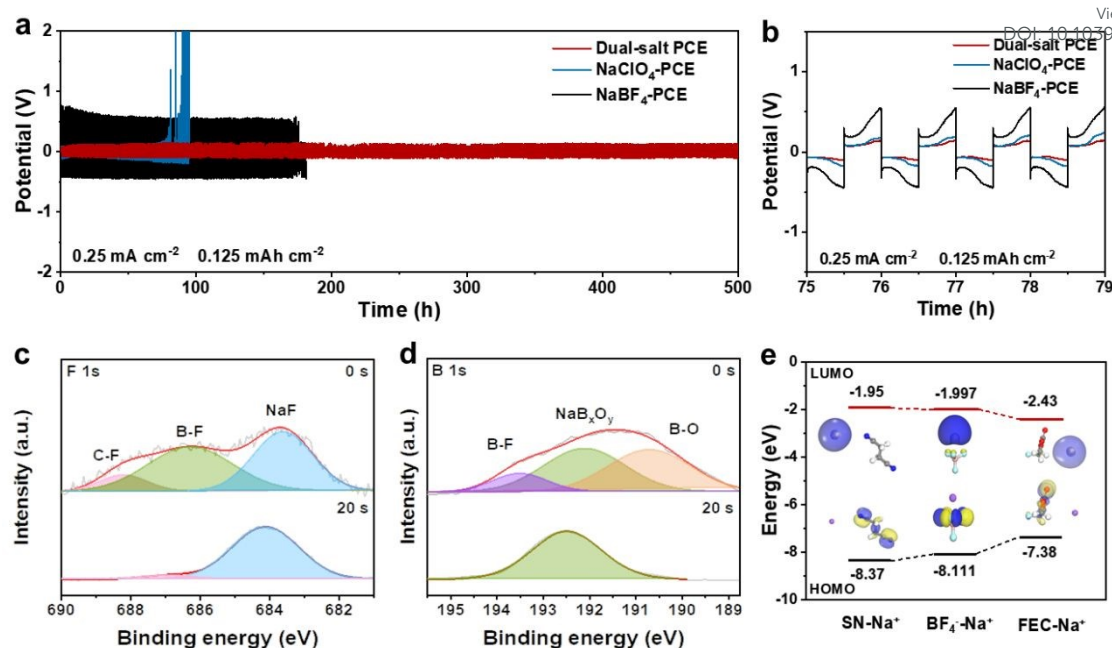


Fig. 3 (a) Voltage profiles of the symmetrical Na||Na cells with dual-salt PCE, NaClO₄-PCE, and NaBF₄-PCE at 0.25 mA cm⁻²/0.125 mAh cm⁻². (b) The enlarged voltage profiles between the 75 and 79 h. XPS depth analysis of (c) F 1s and (d) B 1s for the cycled Na anode in the dual-salt PCE. (e) LUMO/HOMO levels of SN-Na⁺, BF₄⁻ Na⁺, and FEC-Na⁺.



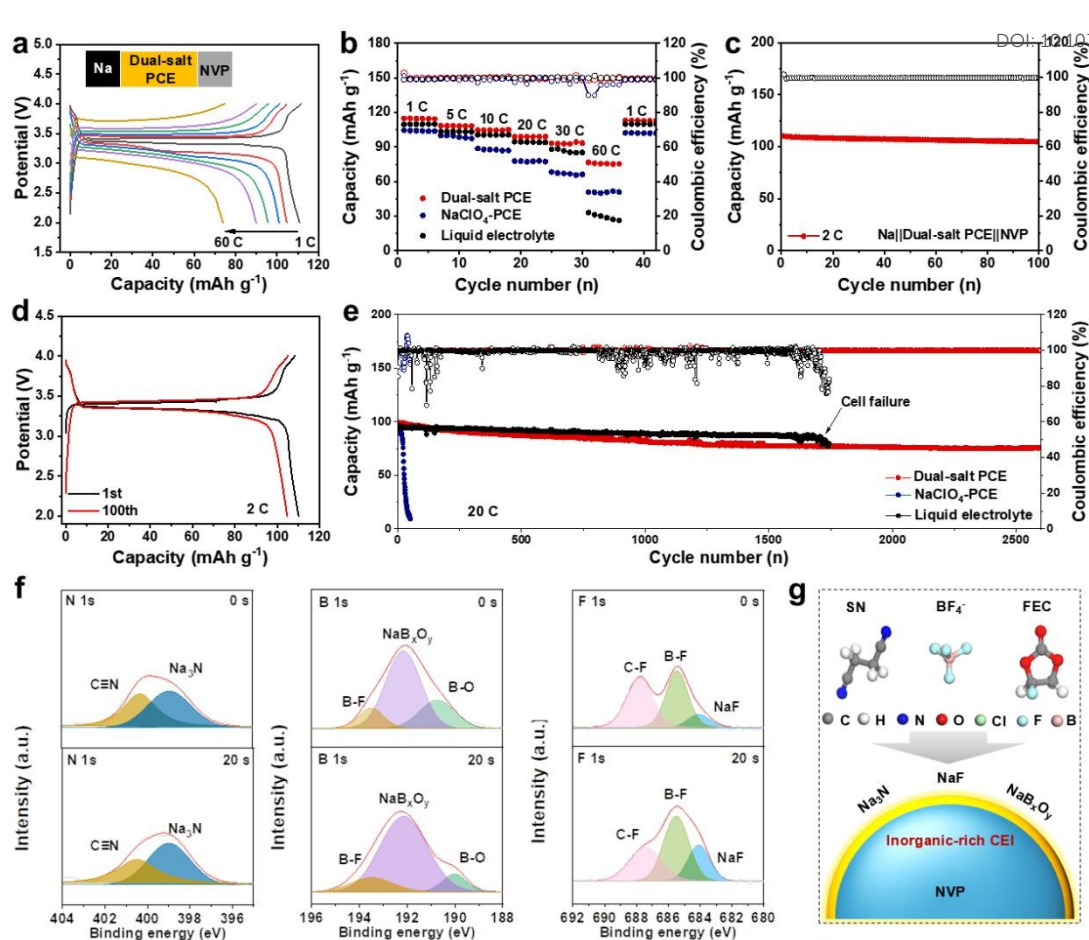


Fig. 4 (a) Charge/discharge profiles of the Na||NVP cell with dual-salt PCE at different rates. (b) Rate performance of the Na||NVP cell with different electrolytes (dual-salt PCE, NaClO₄-PCE, and liquid electrolyte). (c and d) Cycling performance and charge/discharge profiles of the Na||NVP cell at 2 C. (e) Long-term cycling performance of the Na||NVP with different electrolytes at 20 C. (f) In-depth XPS spectra of F 1s, N 1s, and B 1s on the cycled NVP cathode in dual-salt PCE. (g) Schematic diagram of the CEI formation.



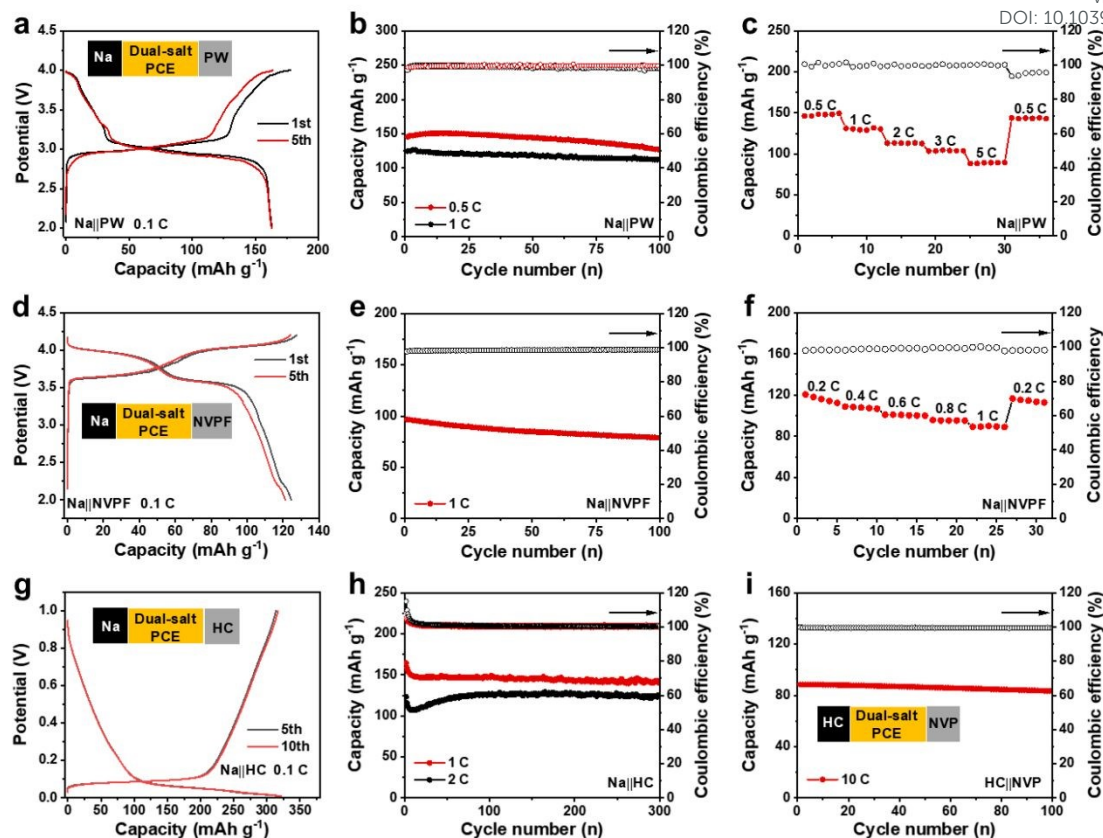


Fig. 5 (a) Charge/discharge profiles of the Na||dual-salt PCE||PW cell at 0.1 C. (b) Cycling performance of the Na||dual-salt PCE||PW cell at 0.5 C and 1 C, respectively. (c) Rate performance of Na||dual-salt PCE||PW cell. (d) Charge/discharge profiles of the Na||dual-salt PCE||NVPF cell at 0.1 C. (e) Cycling performance of the Na||dual-salt PCE||NVPF cell at 1 C. (f) Rate performance of Na||dual-salt PCE||NVPF cell. (g) Charge/discharge profiles of the Na||dual-salt PCE||HC cell at 0.1 C. (h) Cycling performance of the Na||dual-salt PCE||HC cell at 1 C and 2 C, respectively. (i) Cycling performance of the HC||dual-salt PCE||NVP full cell at 10 C.



The data that support the findings of this study are available from the corresponding author upon reasonable request.

